

# Analysis of Current Crowding Effects in Multiturn Spiral Inductors

William B. Kuhn, *Senior Member, IEEE*, and Nouredin M. Ibrahim, *Senior Member, IEEE*

**Abstract**—The effective trace resistance of a multiturn spiral inductor operating at high frequencies is known to increase dramatically above its dc value, due to proximity effect or current crowding. This phenomenon, which dominates resistance increases due to skin effect, is difficult to analyze precisely and has generally required electromagnetic simulation for quantitative assessment. Current crowding is studied in this paper through approximate analytical modeling, and first-order expressions are derived for predicting resistance as a function of frequency. The results are validated through comparisons with electromagnetic simulations and compared with measured data taken from a spiral inductor implemented in a silicon-on-sapphire process.

**Index Terms**—Current crowding, current distribution, inductors, proximity effect, spiral inductor.

## I. BACKGROUND AND INTRODUCTION

**S**PIRAL inductors implemented in silicon processes suffer from several power dissipation mechanisms, leading to poor inductor quality factors. The mechanisms include  $I^2R$  losses from eddy currents circulating below the spiral in the semiconducting substrate, from displacement currents conducted through the turn-to-substrate capacitances and the underlying substrate material, and from the primary inductor current flowing through the thin metal traces of the spiral itself [1]–[4]. In CMOS technologies, the heaviest losses result from eddy currents in the low resistivity substrate (e.g., 0.015  $\Omega$ -cm), often dominating and masking the effects of the latter two mechanisms and limiting  $Q$  to values in the range of three to four [3], [4]. Spirals built in bipolar processes (or bipolar-derived BiCMOS) often exhibit higher  $Q$  values (five to ten) due to relatively high substrate resistivities (e.g., 10–30  $\Omega$ -cm) which reduce eddy currents to negligible values, but may still suffer from significant losses from displacement currents conducted through turn-to-substrate capacitances [3], [5]. These losses can be mitigated by the introduction of a patterned ground shield [6], [7] or by an unpatterned shield of the proper sheet resistance placed below the inductor [8], although at the price of reduced self-resonant frequency.

The best approach to producing high-quality inductors in silicon however, involves etching away the offending semiconducting material below the spiral [9], using a thick oxide layer to separate the spiral from the substrate [10], [11], using a very

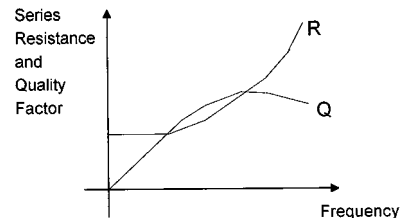


Fig. 1. General form of resistance and  $Q$  for spiral suffering from current crowding.

high resistivity bulk [12], or using an insulating substrate such as sapphire [13]. In such cases, inductor  $Q$ s of 20 and above have been reported, with the highest values found in single turn spirals with values of less than 5 nH.

Unfortunately, for spirals with higher inductances, multiple turns are required and  $Q$  often falls far short of the value that would be predicted from a simple calculation of inductor reactance divided by dc series resistance. The limitation on  $Q$  can be traced to an increase in effective resistance of the metal traces at high frequencies due to skin effect and current crowding [14], [15]. For frequencies below about 2 GHz, skin effects are relatively small in most processes since the trace metal thickness is typically less than or equal to the skin depth. Above 2 GHz, resistance increases associated with skin-effect grow slowly, approaching an asymptote proportional to the square root of frequency. In contrast, current crowding is a strong function of frequency, resulting in resistance increases at a higher than linear rate and a  $Q$  function that is concave downward, as shown in Fig. 1.

Although the problem of current crowding is well known and the general mechanisms involved have been cited and elucidated in several papers [14]–[16], little information is available in the literature to quantitatively predict its magnitude without resorting to numerical simulations [16].

In this paper, we develop a first-order analytical model for the major current crowding mechanisms and derive useful approximate formulas for predicting increases in effective series  $R$  with frequency. Our goal is to provide a framework for understanding the losses involved and to develop simple expressions that can be used to guide explorations of the spiral inductor geometry design space without the need for repeated simulations and/or fabrication and characterization of many spirals. While some steps in the analysis currently rely on empirical expressions (such as that for the normal  $B$  field entering the traces) and others involve simple linearized approximations to higher order functions, the broad framework remains faithful to the physics

Manuscript received March 28, 2000; revised August 22, 2000. This work was supported by the National Science Foundation under Grant ECS-9875770.

W. B. Kuhn is with the Department of Electrical and Computer Engineering, Kansas State University, Manhattan, KS 66506 USA.

N. M. Ibrahim is with Information Technology, Sprint PCS, Lenexa, KS 66219-2301 USA.

Publisher Item Identifier S 0018-9480(01)01554-X.

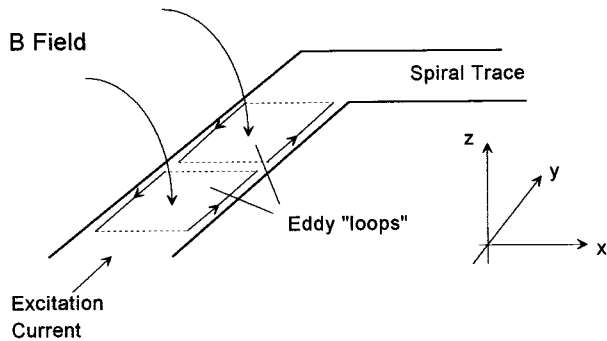


Fig. 2. Illustration of current crowding.

involved, and the predictions made by the model agree well with simulated and measured results.

## II. MODEL DEVELOPMENT

The basic mechanism behind current crowding typically cited in the literature is illustrated in Fig. 2. As the  $B$  field of adjacent turns in the inductor penetrates a trace normal to its surface, eddy currents are produced within the trace that add to the inductor's excitation current on the inside trace edge (nearest the center of the spiral) and subtract from the excitation current on the outside edge. This constricts the current, increasing the effective resistance above the value that would exist for a uniform flow throughout the trace width.

An analysis of this effect requires a sequence of steps that will be undertaken in the following sections, including:

- 1) developing an expression for the normal  $B$  field penetrating the spiral traces;
- 2) calculating the eddy current magnitude (and phase) produced in the traces;
- 3) computing the power losses within the traces due to the addition of the eddy and excitation currents flowing through the nonzero trace resistance;
- 4) comparing this power loss with that expected in the absence of crowding to calculate an effective resistance increase.

### A. Normal $B$ Field Distribution

Arguably, the most difficult analytical step is derivation of the  $B$ -field distribution within the inductor turns. For a circular spiral, a closed form should be possible but would be difficult to work with in subsequent steps. For the more common case of a square spiral, it is doubtful that an exact closed-form result could be obtained with any reasonable amount of effort.

In this paper, we approximate the field distribution by applying the following procedure.

- 1) Solve for the low-frequency normal  $B$  field inside and outside a square filamental conductor.
- 2) Represent the distributed current flow in the actual inductor shown in Fig. 3(a) by a collection of filaments as shown in Fig. 3(b), summing the fields from all filaments of all turns.

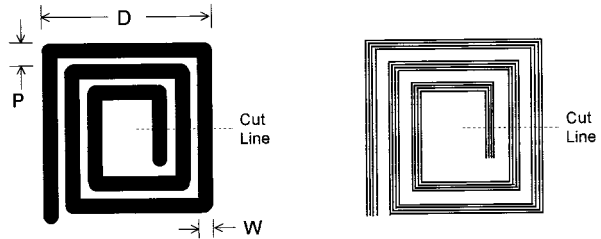


Fig. 3. Spiral geometry and filamentary representation for approximating distributed current.

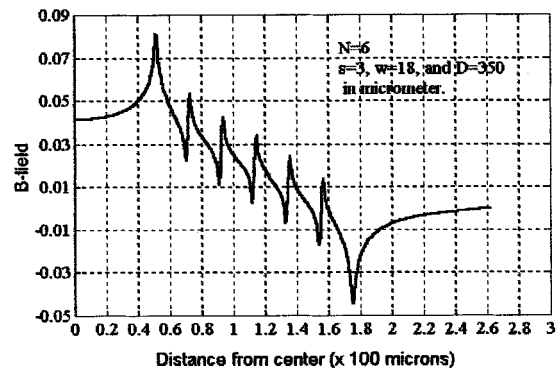


Fig. 4. Calculated  $B$ -field distribution at dc for six-turn, 350- $\mu\text{m}$  square spiral.

- 3) Develop an equation for the field that approximates the calculated field and is suitable for use in subsequent analysis.
- 4) Apply variational principles to address the field redistribution that occurs at high frequencies (discussed in Section II-C).

A numerically computed result for the normal  $B$  field of a six-turn, 350- $\mu\text{m}$  spiral with 18- $\mu\text{m}$ -wide traces, conducting a dc current of 1 A distributed across ten filaments is shown in Fig. 4. The horizontal axis here represents distance from the center of the spiral along the cut-line shown in Fig. 3, while the vertical axis shows  $B$  in SI units.

Note that while the field distribution is complex and varies nonlinearly in the region around the trace edges, the overall shape is a linear increase from a negative value on the outside turn to a positive peak on the inside turn. In the remainder of this paper, we recognize this as a general behavior of multiturn spirals and adopt the following simplified expression for the average  $B$  field in turn  $n$  (numbering from  $n = 1$  at the outside turn):

$$B(n) \approx B_o \left( \frac{n - M}{N - M} \right). \quad (1)$$

Here,  $N$  is the total number of turns,  $B_o$  is the field at the innermost turn ( $N$ ), and  $M$  is the turn number where the field falls to zero and reverses direction.

The magnitude of  $B_o$  and the value of the parameter  $M$  depend on the spiral geometry and the excitation current. The fol-

lowing expression for  $B_o$  has been found to be reasonably accurate for a variety of geometries:

$$B_o \approx 0.65 \frac{\mu_o}{P} I_{\text{ex}}. \quad (2)$$

Here,  $\mu_o$  is the permeability of free space,  $P$  is the turn pitch (see Fig. 3), and  $I_{\text{ex}}$  is the excitation current. Values for  $M$  depend on the degree of spiral fill-in at the center, but a good estimate for typical multiturn geometries with moderate fill is  $M \approx N/4$ .

It should be noted that the expression in (2) is for the region defined by the cut-line shown in Fig. 3. A cut-line through the trace corners yields somewhat higher fields due to proximity to the two sides that meet. This complication will be considered a second-order effect and ignored in subsequent analysis (although it will be seen again in plots of current density in Section III-B).

### B. Eddy Current Magnitude and Phase

Fig. 2, shown previously, suggests that eddy currents add to the spiral's excitation current on the inside edge of a trace and subtract from it on the outside edge. However, careful consideration reveals that the situation is somewhat more complex. At low frequencies, the induced  $E$  field responsible for the eddy current production follows Faraday's law, expressed in point form for the segment of the loop shown in Fig. 2 as

$$\nabla \times E \approx \frac{\partial E_y}{\partial x} = -j\omega B_z. \quad (3)$$

Thus, the  $E$  field and the resulting eddy currents are actually in quadrature with the excitation current, and it is possible for the current magnitude to increase on *both* sides of a trace.

Integration of (3) with respect to  $x$  yields an  $E$  field and resulting eddy current density  $J_{\text{eddy}}$  within a trace of width  $W$ , as illustrated in Fig. 5. Note that a constant of integration has been applied to return the average of the eddy current to zero, so that the total current in the trace remains equal to the current  $I_{\text{ex}}$  applied at the spiral's terminals.<sup>1</sup>

To simplify subsequent expressions in the analysis, we will approximate  $B(n)$  as constant across trace  $n$ , as illustrated by the dotted line, yielding a first-order expression for  $E$  of the form

$$E(x) = -j\omega B(n)x \quad \text{for} \quad -W/2 \leq x \leq W/2 \quad (4)$$

and an eddy current density at the trace edges with a magnitude of

$$|J_{\text{eddy}}| = \sigma E = \sigma\omega B(n) \frac{W}{2} \quad (5)$$

where  $\sigma$  is the conductivity of the trace metal. Taking the ratio of (5) to the excitation current density in the trace, which is as-

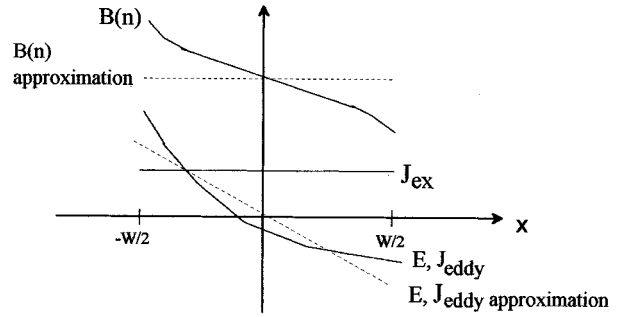


Fig. 5. Excitation current,  $B$  field, and induced  $E$  field and eddy currents profiles within trace.

sumed to have a thickness  $T$ , yields

$$\left| \frac{J_{\text{eddy}}}{J_{\text{ex}}} \right| = \frac{B(n) \frac{W}{2} \sigma \omega}{I_{\text{ex}} / (WT)} \quad (6)$$

which can be combined with (1) and (2) to yield

$$\left| \frac{J_{\text{eddy}}}{J_{\text{ex}}} \right| = \frac{0.65}{2} \mu_o \sigma \omega T \frac{W^2}{P} \frac{(n-M)}{(N-M)}. \quad (7)$$

This expression is maximum at the innermost turn ( $n = N$ ) and, if set to one for this case, can be used to find the frequency  $\omega_{\text{crit}}$  at which the current crowding begins to become significant

$$\omega_{\text{crit}} = \frac{3.1}{\mu_o} \frac{P}{W^2} R_{\text{sheet}}. \quad (8)$$

Here, the trace's sheet resistance  $R_{\text{sheet}}$  has been used in place of  $1/(\sigma T)$  to make the expression more user friendly to the IC designer.

Evaluation of (8) with  $W$  and  $P$  set to representative values of 18 and 20  $\mu\text{m}$  and with  $R_{\text{sheet}}$  set to 0.02  $\Omega/\square$  reveals that the onset of current crowding can easily occur at frequencies below 500 MHz. The expression also points to the fact that the onset of eddy currents occurs at even lower frequencies as the metal resistance decreases. However, it should not be concluded that this will negate the advantage of using lower sheet resistance. Equation (8) only shows when the resistance of the spiral will start to increase. Lower  $R_{\text{sheet}}$  should still yield  $Q$  improvements in proportion to the reduction in  $R_{\text{sheet}}$  for frequencies up to approximately  $\omega_{\text{crit}}/2$  and somewhat less improvement at higher frequencies.

### C. Field Redistribution at High Frequencies

The expressions derived above assume that the  $B$  field distribution within the inductor remains unchanged from the low-frequency distribution assumed in (1) and Fig. 5. At high frequencies, this assumption must be reexamined.

For a multiturn spiral, the field at turn  $n$  is the superposition of fields from all turns. Thus, while eddy currents flowing in adjacent turns will produce some modification to  $B(n)$ , the field contributions from equal and opposite eddy currents along the edges of other turns will largely cancel at turn  $n$ , and the net contribution from all turns will be relatively unchanged at low fre-

<sup>1</sup>The average current in the traces equals the terminal excitation current for frequencies well below the spiral's self-resonant frequency (SRF). As the SRF is approached, some modifications would be required. Thus, the following analysis is limited to use below the SRF.

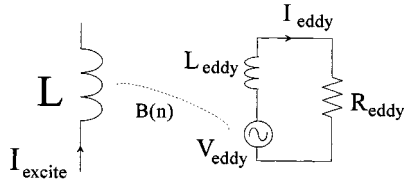


Fig. 6. Lumped element model of single eddy current "loop" of Fig. 2.

quencies. For frequencies well above  $\omega_{\text{crit}}$ , however, the presence of large eddy currents along the edges of adjacent turns, and especially along the edges of turn  $n$  itself, can significantly change the field in turn  $n$ . To illustrate this, and to approximately quantify the effect, refer to the circuit model of Fig. 6.

Here,  $V_{\text{eddy}}$  represents the voltage induced in an eddy loop within turn  $n$  by the field  $B(n)$  produced from the complete spiral.  $I_{\text{eddy}}$  represents the average eddy current along the trace edge and  $R_{\text{eddy}}$  represents the net resistance through which this current flows. The effect of field redistribution within the turn  $n$  is modeled by  $L_{\text{eddy}}$  which develops back electromotive force, limiting  $I_{\text{eddy}}$  at high frequencies and changing the phase of the eddy currents from quadrature to in-phase with  $I_{\text{excite}}$  when the reactance of  $L_{\text{eddy}}$  sufficiently exceeds  $R_{\text{eddy}}$ .

To roughly quantify these effects, we note from (4) that eddy currents are concentrated near the edges of the trace. We represent the current on each edge approximately by a uniform current [equal to that given in (5)] flowing within the outer 25% of the trace width. Approximate expressions for  $L_{\text{eddy}}$  and  $R_{\text{eddy}}$  can then be adapted from transmission line and sheet resistance formulas as<sup>2</sup>

$$L_{\text{eddy}} \approx \frac{\mu_0}{\pi} \ln \left( \frac{W}{W/4} \right) l \quad (9)$$

$$R_{\text{eddy}} \approx \frac{2R_{\text{sheet}}}{W/4} l \quad (10)$$

where  $l$  is the length of the eddy loop in the  $y$  direction. Taking the ratio of  $R_{\text{eddy}}$  to  $L_{\text{eddy}}$  then gives an estimate for the frequency where the limiting of eddy currents reaches 3 dB and the phase relationship of  $I_{\text{eddy}}$  to  $I_{\text{ex}}$  reaches  $45^\circ$

$$\omega_{\text{lim}} \approx 18 \frac{1}{\mu_0 W} R_{\text{sheet}}. \quad (11)$$

This is approximately four to six times  $\omega_{\text{crit}}$  given in (8) for the case of spirals with  $W \approx P$ . As an example, for a 350- $\mu\text{m}$  six-turn 10-nH inductor with a trace width of 18  $\mu\text{m}$  and a pitch of 20  $\mu\text{m}$ , and  $R_{\text{sheet}} = 0.02 \Omega/\square$ ,  $\omega_{\text{crit}} \approx 3 \text{ Gr/s}$  (480 MHz), and  $\omega_{\text{lim}} \approx 16 \text{ Gr/s}$  (2.5 GHz). Between these frequencies, eddy currents steadily build with frequency and have an approximately quadrature phase relationship, as previously described.

As a final note, we recognize that the field distribution given by (1) and (2) will also be modified when the spiral approaches self-resonance. In this case, the excitation current along the spiral will not remain in-phase with the terminal currents, and appropriate modifications will be required in (1) and (2). This

<sup>2</sup>The expression in (9) is the value of  $L$  for a two-wire transmission line and is not strictly applicable here. However, it provides a useful first-order estimate to the relatively complex situation under construction.

complication will be treated in subsequent work and will not be addressed here.

#### D. Estimation of Resistance Increases with Frequency

Previous results can now be combined to approximate the effective series resistance  $R_{\text{eff}}$  of the spiral versus frequency. This will be done by setting  $I_{\text{ex}}^2 R_{\text{eff}}$  equal to the power dissipated. To simplify the analysis, we shall assume that the frequency of operation is below  $\omega_{\text{max}}/2$  so that  $I_{\text{ex}}$  and  $I_{\text{eddy}}$  can be assumed to be in phase quadrature and the power dissipation from each can be computed independently.

The power dissipated in the  $n$ th turn is then

$$P_n = I_{\text{ex}}^2 R_n + I_{\text{eddy}}^2 R_{\text{eddy}_n} \quad (12)$$

where  $R_n$  is the dc resistance of turn  $n$  and  $R_{\text{eddy}_n}$  is the resistance through which the eddy current flows in turn  $n$ .  $R_n$  can be found from the sheet resistance  $R_{\text{sheet}}$  and the length of the turn  $l_n$  as

$$R_n = R_{\text{sheet}} \frac{l_n}{W} \quad (13)$$

while the eddy current  $I_{\text{eddy}}$  and the resistance  $R_{\text{eddy}_n}$  through which it flows can be estimated using the approach outlined in the previous section as

$$I_{\text{eddy}} \approx J_{\text{eddy}} \frac{W}{4} T \quad (14)$$

$$R_{\text{eddy}_n} \approx 2R_{\text{sheet}} \frac{l_n}{W/4} = 8R_n \quad (15)$$

and where  $J_{\text{eddy}}$  is the current given in (5) and  $T$  is the trace thickness.

Combining (12)–(15) with (1), (2), and (5) then gives

$$P_n \approx I_{\text{ex}}^2 R_n + \left[ 0.65 \omega \frac{W^2}{8} \sigma T \frac{\mu_0}{P} \left( \frac{n-M}{N-M} \right) I_{\text{ex}} \right]^2 8R_n \quad (16)$$

which can be combined with (8) and written in terms of  $\omega_{\text{crit}}$  (after replacing  $\sigma T$  by  $1/R_{\text{sheet}}$ ) as:

$$P_n \approx I_{\text{ex}}^2 R_n \left[ 1 + \frac{1}{2} \left( \frac{\omega}{\omega_{\text{crit}}} \right)^2 \left( \frac{n-M}{N-M} \right)^2 \right]. \quad (17)$$

Equation (17) provides several useful insights. For example, the term in brackets represents the factor by which the resistance of turn  $n$  is increased due to eddy currents. For the innermost turn, this resistance doubles by the time the frequency of operation reaches  $\omega = \sqrt{2}\omega_{\text{crit}}$ . For other turns, the doubling is delayed due to the weaker fields. In addition, the effective resistance for all turns, and hence for the complete inductor, follows a quadratic curve with increasing frequency (up to the vicinity of  $\omega_{\text{max}}/2$ ).

To find an expression for the total spiral resistance  $R_{\text{eff}}$ , (17) can be summed over  $n$  and the result equated to  $I_{\text{ex}}^2 R_{\text{eff}}$  to give

$$R_{\text{eff}} \approx R_{\text{DC}} + \frac{1}{2} \left( \frac{\omega}{\omega_{\text{crit}}} \right)^2 \sum_{n=1}^N R_n \left( \frac{n-M}{N-M} \right)^2 \quad (18)$$

where  $R_{\text{DC}}$  is the spiral's series resistance at dc and the terms within the summation are geometry dependent. A plot of this

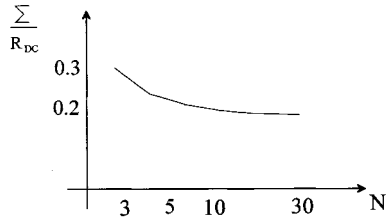


Fig. 7. Plot of sum term in (18) versus number of turns for spiral with 2/3 fill-in.

sum divided by  $R_{DC}$  for the typical case of a spiral with the inner third unfilled is shown in Fig. 7, from which a nominal value of  $0.2 R_{DC}$  can be taken to yield the following result for simple rough estimates of  $R_{eff}$

$$R_{eff} \approx R_{DC} \left[ 1 + \frac{1}{10} \left( \frac{\omega}{\omega_{crit}} \right)^2 \right]. \quad (19)$$

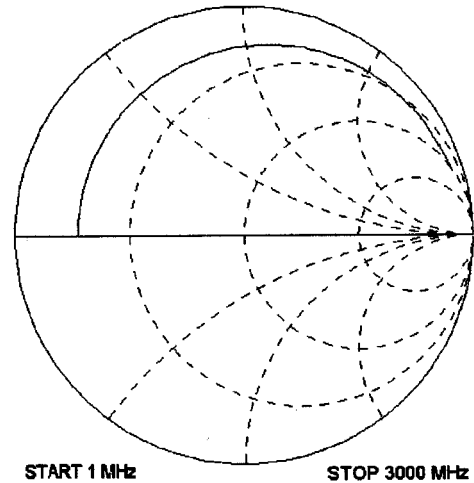
### III. MODEL VALIDATION

The quantitative predictions of current crowding offered by (8), (11), and (19) are compared in this section with measured data and electromagnetic simulation results to assess the validity and accuracy of the analytic model. The measured data used in the validation is taken from a six-turn spiral fabricated in a silicon-on-sapphire (SOS) process. The data are fit to a lumped-element circuit model to extract the spiral's series resistance versus frequency. They are then compared against the analytic model's predictions of a 10% increase in resistance at  $\omega_{crit}$ , a quadratic rise in  $R$  with frequency, and a leveling out of series resistance in the vicinity of  $\omega_{lim}$ . Data generated with a commercial electromagnetic simulator (Agilent EEs of Momentum) are then used to assess predictions of these behaviors over a range of widths, pitches, turns, and sheet resistance values. Finally, simulated plots of current density within the spiral traces are examined to check the  $B$  field distribution of (1), the eddy current distribution of Fig. 5, and the eddy current to excitation current phase relationships predicted by the model of Fig. 6.

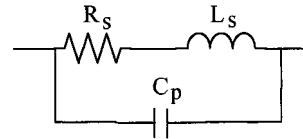
#### A. Comparison with Measured Results

Raw S11 data taken from a 9.5-nH inductor using Cascade Microtech coplanar waveguide probes connected to an HP8753A network analyzer are shown in Fig. 8(a). The measurements are from a traditional square spiral with dimensions of  $D = 350 \mu\text{m}$ ,  $N = 5.75$ ,  $W = 18 \mu\text{m}$ , and  $P = 21 \mu\text{m}$ , fabricated in an SOS process with metal sheet resistance  $R_{sheet} \approx 0.028 \Omega/\square$  (representing the effective value after stacking the three available metal layers). This data were then fit to the model shown in Fig. 8(b) [13] to separate the actual series inductance and resistance from the apparent values created by parallel capacitance between turns and within the probe pad structure.

The graphs in Fig. 9(a) and (b) show the apparent  $R$  and  $L$  values computed directly from S11 and the values found after fitting to the model of Fig. 8(b), respectively. The apparent  $L$  value of Fig. 9(a) is computed as the imaginary part of the



(a)



(b)

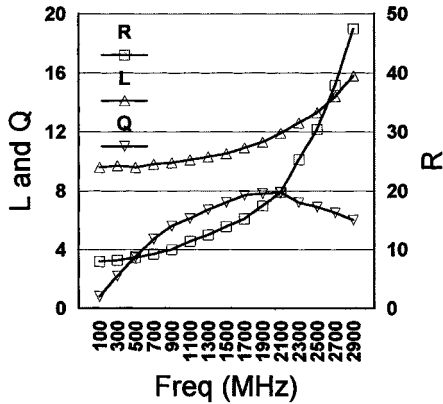
Fig. 8. (a) S11 measurements and (b) model used to extract series  $R$  versus frequency.

measured impedance  $Z$  divided by  $2\pi f$ , while the apparent  $R$  value represents the real part of  $Z$  directly. Both quantities rise with frequency as self-resonance is approached on the right side of the Smith chart. The resistance and inductance shown in Fig. 9(b) represent  $R_s$  and  $L_s$  in the lumped-element model of Fig. 8(b) after  $C_p$  is found and fixed at a constant value. The virtually constant value of  $L$  versus frequency shown confirms the fit of the model to the data throughout the frequency range. Values for inductor quality factor (computed as  $X_L/R$ ) are also plotted in both graphs.

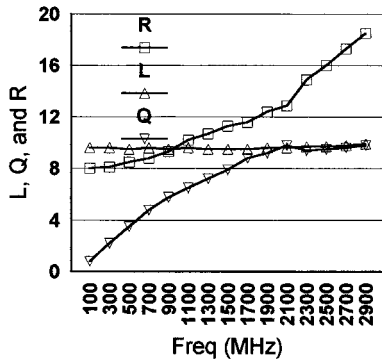
Inspection of Fig. 9(b) shows good agreement with the predictions of the analytic model developed in previous sections. Equation (8) predicts a critical frequency of 710 MHz for this spiral, while (19) predicts that the resistance will up by 10% at this frequency and rise at a quadratic rate. Fig. 9(b) shows a resistance increase of 10% at approximately 700 MHz, and an increase of 40% at approximately 1500 MHz, verifying both predictions. Equation (11) and the theory surrounding it predict that resistance increase will begin to level out in the neighborhood of 3.2 GHz, while the measured results show that the quadratic increase in resistance has slowed to linear by 2.9 GHz, the upper frequency range of measurement.

#### B. Comparison with Simulation Results

To validate the analytic model over a range of values for  $W$ ,  $P$ ,  $N$ , and  $R_{sheet}$ , electromagnetic simulations were run for the following cases (all have  $D = 350 \mu\text{m}$ ):



(a)



(b)

Fig. 9. Measured parameters (a) before and (b) after fitting to the model of Fig. 8(b).

Case 1)  $N = 6$ ,  $W = 18 \mu\text{m}$ ,  $P = 21 \mu\text{m}$ , and  $R_{\text{sheet}} = 0.028 \Omega/\square$  [9.5 nH]

Case 2) Same as Case 1), but with  $R_{\text{sheet}} = 0.014 \Omega/\square$  [9.5 nH]

Case 3) Same as Case 1), but with  $W$  decreased to  $12 \mu\text{m}$  [9.4 nH]

Case 4)  $N = 3$ ,  $W = 38 \mu\text{m}$ ,  $P = 42 \mu\text{m}$ , and  $R_{\text{sheet}} = 0.028 \Omega/\square$  [2.6 nH]

Case 5) Same as Case 4), but with  $R_{\text{sheet}}$  increased to  $0.056 \Omega/\square$  [2.6 nH]

Case 6) Case 6:  $N = 12$ ,  $W = 8.5 \mu\text{m}$ ,  $P = 10.5 \mu\text{m}$ , and  $R_{\text{sheet}} = 0.028 \Omega/\square$  [35 nH]

For each case, the simulated S11 values were fit to the model of Fig. 8(b) and the series resistance versus frequency was found as described earlier. The results, expressed as resistance at frequency  $f$  divided by resistance at dc, are shown in Fig. 10, and the predictions of critical frequency and limiting frequency from (8) and (11) for each case are shown in Table I. The values of critical frequency from Table I agree with the intercept points of the line  $R/R_{\text{dc}} = 1.1$ , as predicted by (19). In addition, all curves show the expected square-law behavior of resistance, and evidence of limiting at high frequency can be seen.

There is some quantitative discrepancy, however, between the measured results shown previously in Fig. 9(b) and the data for Case 1) (which is designed to match the measured spiral) and

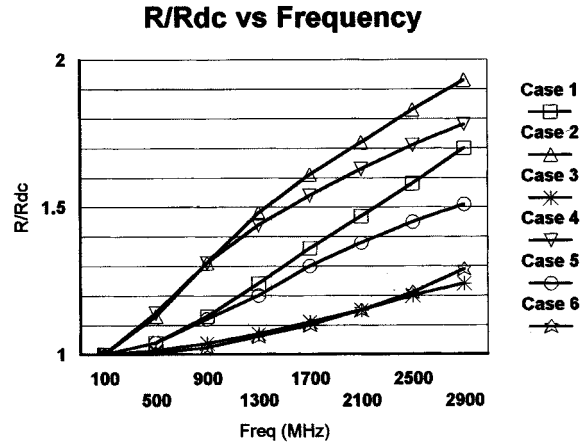


Fig. 10. Spiral resistance divided by dc value for six different cases.

TABLE I  
PREDICTED VALUES OF CRITICAL FREQUENCY AND LIMITING  
FREQUENCY FOR SIX CASES

Case	1	2	3	4	5	6
Critical $f$ (MHz)	710	360	1,600	320	640	1,600
Limiting $f$ (MHz)	2,500	1,800	5,300	1,700	3,400	7,500

between the frequency of limiting predicted in Table I and the inflection points shown in the plots of Fig. 10. The former is believed to be due to stacking of metal layers to achieve a low composite resistance in the measured spiral (with some minor contribution also due to skin effects, which are not included in the simulations). This behavior of stacked-metal spirals has been previously observed in the literature [11]. The latter problem is believed to be due to approximations made in deriving (11) and indicates that further work is needed to provide good quantitative modeling of resistance increase at frequencies well above  $\omega_{\text{crit}}$ .

Finally, the general behavior of eddy current development and the phase relationships assumed in deriving (8), (11), and (19) were checked by plotting current density within the spiral traces. Fig. 11 shows the current magnitude in the spiral traces at two different phases of the excitation current, with lighter areas representing larger instantaneous magnitudes. Fig. 11(a) shows the case for the excitation phase that results in a peak value on the inside edge of the inner trace, while Fig. 11(b) shows the case for the phase that results in zero instantaneous current at this same location. The meshing used in the electromagnetic simulations can be seen in both.

From Fig. 11(a), the effects of the  $B$  field distribution shown previously in Fig. 4 can be seen. For the inner turns, the field, and hence the eddy currents, are maximum on the inside of the trace, while for the the outer turn, the field is reversed and the eddy current maximum occurs on the outside of the trace. As expected from the assumed  $B$  field distribution of (1), the general progression of eddy currents is a linear decrease for turns farther from the center of the spiral falling to approximately zero in the neighborhood of turn 2 to 3, and then reversing direction (maximum current crowding on outside edge of outside turn).

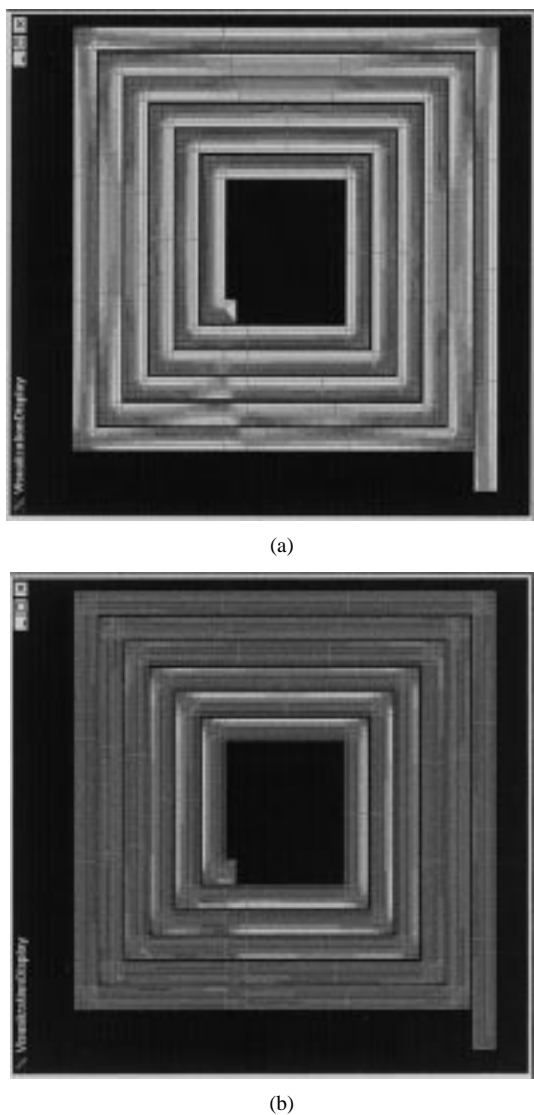


Fig. 11. Current density magnitudes within inductor traces at  $\omega_{\text{crit}}$  at (a) excitation phase resulting in peak value on inside of inner turn and (b) at phase resulting in zero instantaneous current on inside of inner turn.

A comparison of Fig. 11(a) and (b) also agrees with the conclusion that eddy currents flow in opposite directions on the two sides of the trace and are approximately in quadrature with the excitation current at lower frequencies. If the currents flowed in-phase with the excitation current, then the plot of Fig. 11(b) would be uniformly dark, indicating zero instantaneous current at all points simultaneously. Instead, the lighter shading on the outside edge of the inner turn trace shows significant current at this point, indicating that the eddy currents on the two edges are not in-phase (or antiphase) at this frequency. The fact that the outside edge does not reach the same peak magnitude as the inside edge at this phase is attributed to the increasing  $B$  field across the trace shown in Figs. 3 and 4—a factor that was successfully abstracted out of the model to keep the derivation of (4)–(8) and the result in (19) simplified.<sup>3</sup>

<sup>3</sup>Additional plots of this type, cycling through 16 phase points, showed that the outside edge does peak approximately  $90^\circ$  from the inside edge peak (as would be suggested by the theory at  $\omega_{\text{crit}}$  where  $J_{\text{eddy}} = J_{\text{ex}}$ ), while plots at high frequency (above  $\omega_{\text{lim}}$ ) showed a nearly in-phase relationship, in agreement with the model of Fig. 6.

#### IV. SUMMARY AND CONCLUSIONS

Previous work with spiral inductors fabricated in technologies with insulating or very high-resistivity substrates have shown significant increases in series resistance at high frequency. This problem is especially severe in inductors used in low power designs operating at low gigahertz frequencies, where multiturn spirals with moderate  $L$  values are needed. While the general mechanisms behind the current crowding mechanism responsible are well known, previous authors have considered the problem too difficult to address analytically, and no simple theory has been available to help in exploring the inductor design space. Equations (8), (11), and (19) derived in this paper provide an approximate analytic model for current crowding effects. These expressions can be used to obtain first-order estimates of the frequency  $\omega_{\text{crit}}$  at which resistance increases begin and thus to understand the general quantitative as well as qualitative form of the increase in  $R$  with frequency.

The model's predictions of  $\omega_{\text{crit}}$  and of the square-law increase in  $R$  have been found to be accurate over a significant range of values for trace width, pitch, number of turns, and metal sheet resistance. Prediction of the frequency  $\omega_{\text{lim}}$  at which the increase in resistance slows due to redistribution of the magnetic fields within the spiral is less precise, indicating the need for more detailed modeling of these effects. However, plots of current density within the spiral traces are in general agreement with the major features of the theory, suggesting that this effect may also be accessible to analytical modeling, and that the general procedures adopted in this paper should be extendable to other spiral inductor and transformer geometries.

#### ACKNOWLEDGMENT

The authors wish to acknowledge that spiral inductor fabrication was performed through MOSIS. Electromagnetic simulations were made possible by a donation of EEs of EDA tools from Agilent (formerly Hewlett-Packard).

#### REFERENCES

- [1] N. M. Nguyen and R. G. Meyer, "Si IC-compatible inductors and LC passive filters," *IEEE J. Solid-State Circuits*, pp. 1028–1031, Aug. 1990.
- [2] C. P. Yue, C. Ryu, J. Lau, T. H. Lee, and S. S. Wong, "A physical model for planar spiral inductors on silicon," in *Proc. IEEE Int. Electron Devices Meetings*, 1996, pp. 155–158.
- [3] J. R. Long and M. A. Copeland, "The modeling, characterization, and design of monolithic inductors for silicon RF IC's," *IEEE J. Solid-State Circuits*, pp. 357–369, Mar. 1997.
- [4] W. B. Kuhn and N. K. Yanduru, "Spiral inductor substrate loss modeling in silicon RFICs," *Microwave J.*, pp. 66–81, March 1999.
- [5] J. N. Burghartz, M. Soyuer, and K. A. Jenkins, "Integrated RF and microwave components in BiCMOS technology," *IEEE Trans. Electron Devices*, pp. 1559–1570, 1996.
- [6] C. P. Yue and S. S. Wong, "On-chip spiral inductors with patterned ground shields for Si-based RF IC's," *IEEE J. Solid-State Circuits*, pp. 743–752, May 1998.
- [7] F. Mernyei, F. Darrer, M. Pardo, and A. Sibrai, "Reducing the substrate losses of RF integrated inductors," *IEEE Microwave Guided Wave Lett.*, pp. 300–301, 1998.
- [8] W. B. Kuhn and N. K. Yanduru, "Spiral inductor substrate loss modeling in silicon RFICs," in *Proc. IEEE Radio Wireless Conf.*, 1998, pp. 305–308.
- [9] J. Y.-C. Chang, A. A. Abidi, and M. Gaitan, "Large suspended inductors on silicon and their use in a 2- $\mu\text{m}$  CMOS RF amplifier," *IEEE Electron Device Lett.*, pp. 246–248, May 1993.

- [10] J. N. Burghartz, M. Soyuer, K. A. Jenkins, and M. D. Hulvey, "High- $Q$  inductors in standard silicon interconnect technology and its application to an integrated RF power amplifier," in *Proc. Int. Electron Devices Meeting*, 1995, pp. 29.8.1–29.8.3.
- [11] J. N. Burghartz, M. Soyuer, and K. A. Jenkins, "Microwave inductors and capacitors in standard multilevel interconnect silicon technology," *IEEE Trans. Microwave Theory Tech.*, pp. 100–104, Jan. 1996.
- [12] K. B. Ashby, I. A. Koullias, W. C. Finley, J. J. Bastek, and S. Moinian, "High  $Q$  inductors for wireless applications in a complementary silicon bipolar process," *IEEE J. Solid-State Circuits*, pp. 4–9, Jan. 1996.
- [13] R. A. Johnson, C. E. Chang, P. M. Asbeck, M. E. Wood, G. A. Garcia, and I. Lagnado, "Comparison of microwave inductors fabricated on silicon-on-sapphire and bulk silicon," *IEEE Microwave Guided Wave Lett.*, pp. 323–325, Sept. 1996.
- [14] J. Craninckx and M. S. J. Steyaert, "A 1.8-GHz low-phase-noise CMOS VCO using optimized hollow spiral inductors," *IEEE J. Solid-State Circuits*, pp. 736–744, May 1997.
- [15] H.-S. Tsai, J. Lin, R. C. Frye, K. L. Tai, M. Y. Lau, D. Kossives, F. Hrycenko, and Y.-K. Chen, "Investigation of current crowding effect on spiral inductors," in *Proc. IEEE MTT-S Int. Topical Symp. Technologies for Wireless Applications*, 1997, pp. 139–142.
- [16] A. M. Niknejad and R. G. Meyer, "Analysis, design, and optimization of spiral inductors and transformers for Si RF IC's," *IEEE J. Solid-State Circuits*, pp. 1470–1481, Oct. 1998.



**Nouredin M. Ibrahim** (SM'00) was born in Qena Province, Egypt, in 1959. He received the B.S. (first in class with honor) and M.S. degrees in electrical engineering from Assiut University, Assiut, Egypt, in 1982 and 1987, respectively, and the Ph.D. degree from Minia University, Minia, Egypt, in 1995. He is currently pursuing the M.S. degree in RF microelectronics at Kansas State University, Manhattan.

In 1982, he joined the Department of Electrical Engineering, Assiut University to help in teaching while working toward the M.S. degree. From 1983 to 1984, he temporarily joined the Department of Defense of Egypt as a Radar Engineer. In 1984, he returned to Assiut University. In 1988, he joined Minia University as an Associate Lecturer in RF systems, electromagnetics, antennas and wave propagation, telecommunications, signal processing, mathematics, and microelectronics. In 1991, he joined the National Research Council of Canada. He then returned to Minia University, where he became an Assistant Professor. In 1999, he joined Sprint Corporation, Lenexa, KS, where he is a Telecommunications Engineer. He has published in international journals in fiber-optics, RF systems, and engineering education.



**William B. Kuhn** (S'78–M'79–SM'98) was born in Newport News, VA, in 1956. He received the B.S. degree in electrical engineering and the Ph.D. degree from Virginia Polytechnic Institute and State University, Blacksburg, VA, in 1979 and 1996, respectively, and the M.S. degree in electrical engineering from the Georgia Institute of Technology, Atlanta, in 1982.

From 1979 to 1981, he was with Ford Aerospace and Communications Corporation, Palo Alto, CA, where he designed radio receiver equipment including frequency synthesizers and bit synchronizers. From 1983 to 1992, he was with the Georgia Tech Research Institute, Atlanta, working primarily in radar signal analysis and mixed-signal circuit simulator development. In 1996, he joined Kansas State University, Manhattan, as an Assistant Professor, where he became an Associate Professor in 2000. He currently teaches courses in linear systems, radio and microwave engineering, and VLSI design and is involved in research on full integration of low-power radio electronics in CMOS and BiCMOS technologies.

Dr. Kuhn received the Bradley Fellowship from Virginia Tech in 1993 and a Faculty Early Career Development (CAREER) award from the National Science Foundation in 1999.